coatings

MDPI

Article

Physical-Vapor-Deposition-Coated Natural Rocks as Sustainable Cutting Material: First Insights into the Effect of Substrate Integrity on Properties of TiN Thin Film

Hilke Petersen [1,*], Dominic Graf [2], Nelson Filipe Lopes Dias [2], Wolfgang Tillmann [2], Philipp Dan Hendrik Wolters [1], Benjamin Bergmann [1] and Bernd Breidenstein [1]

[1] Institute of Production Engineering and Machine Tools (IFW), Leibniz University Hannover, An der Universität 2, 30823 Garbsen, Germany; breidenstein@ifw.uni-hannover.de (B.B.)
[2] Institute of Materials Engineering, TU Dortmund University, Leonhard-Euler-Straße 2, 44227 Dortmund, Germany
* Correspondence: hilke.petersen@ifw.uni-hannover.de

Abstract: The most important cutting materials for machining are carbides. Their production requires both tungsten and cobalt; however, these materials are becoming increasingly difficult to obtain and are sometimes mined under ethically questionable conditions. As a result, increasing efforts are being made to expand the range of cutting materials. The basic suitability of natural rocks for cutting tools in less demanding processes has already been demonstrated. PVD coating of the natural rocks could improve their performance. The adhesion mechanisms in TiN-coated natural rock samples are discussed below. The TiN thin film is characterized in depth.

Keywords: physical vapor deposition; titanium nitride; cutting materials; rocks; adhesion

Citation: Petersen, H.; Graf, D.; Lopes Dias, N.F.; Tillmann, W.; Wolters, P.D.H.; Bergmann, B.; Breidenstein, B. Physical-Vapor-Deposition-Coated Natural Rocks as Sustainable Cutting Material: First Insights into the Effect of Substrate Integrity on Properties of TiN Thin Film. *Coatings* **2024**, *14*, 1333. https://doi.org/10.3390/coatings14101333

Academic Editors: Aleksander Lisiecki and Agnieszka Kurc-Lisiecka

Received: 9 September 2024
Revised: 11 October 2024
Accepted: 16 October 2024
Published: 17 October 2024

1. Introduction

Cemented carbide is the most commonly used cutting material; however, its production is economically and energetically costly [1]. In particular, the contained elements cobalt and tungsten are becoming increasingly scarce. The main areas for the mining of these materials are limited to a few world regions, and their production mostly occurs under ethically problematic circumstances [2–4]. Consequently, academic and industrial research is focusing on exploring new materials to expand the range of cutting materials. Here, natural rocks have proved to be an interesting possibility [5,6]. Natural rocks combine various ecological and economic advantages. Compared to conventional cutting materials, their production is more energy efficient, as many energy-intensive process steps for forming the raw material of rocks are already performed in nature and solely the geometrical preparation of the tools has to be considered. The properties of the rocks depend primarily on their mineral composition, structure, and texture, which, in turn, are characterized by the formation process of the rock [7,8]. However, natural rocks have a heterogeneous structure consisting of various phases, which must be considered during their production and application as cutting materials. Additionally, the phase composition can vary depending on the extraction location, and this variability should be further considered when manufacturing cutting tools from natural rocks [7]. In principle, a distinction is made between igneous, sedimentary, and metamorphic rocks [7]. Igneous rocks are formed through the solidification of molten rock mass. Sedimentary rocks form via the sedimentation of smaller rocks and by precipitation of chemical compounds from solutions. Metamorphic rocks emerge from the transformation processes of magma and sedimentary rock under high temperatures and pressures. The materials studied here are flint (sedimentary rock), lamellar obsidian (igneous rock), alta-quartzite, silver-quartzite (metamorphic rock), and the mineral quartz. These materials are characterized by their

high SiO_2 content of over 90 wt.%. An exception is the mineral quartz, which consists purely of highly crystalline SiO_2. Flint is a highly crystalline, isotropic solid. In contrast, the lamellar obsidian has a glassy, layered structure. Both quartzites (alta- and silver-) have a layered structure. X-ray powder diffraction analysis of quartzites shows layered aluminosilicates as a secondary phase [6].

The machinability of various rocks for the production of cutting tools has already been demonstrated in previous works [5,6,9–12]. Various correlations between the mechanical and microstructural properties of the rocks and their machinability were identified. In particular, the flexural strength, hardness, and texturing of the rocks proved to be reliable parameters for judging the possible suitability of rocks as cutting materials. Furthermore, relevant process parameters for the machining of cutting inserts via grinding were determined. In the grinding experiments, metallic-bonded diamond grinding wheels showed the best performance. In addition, the different rock types have a significant influence on the flank roughness and the achievable sharpness, as well as the cutting-edge geometry. The axial feed rate correlates with the sharpness. The cutting material grain concentration influences the flank roughness and the sharpness, while the grain size also influences the cutting-edge rounding. For this reason, it is advisable to use grinding tools with small grain sizes and higher grain concentrations. In addition, the fundamental suitability of rocks as cutting materials for machining softer materials such as plastics and aluminum alloys could be demonstrated [9]. The study of the process parameters showed similar correlations with the process forces principles compared to conventional materials of indexable inserts.

Scratch studies showed that, with suitable precision cutting thicknesses of ~2.5 µm and cutting speeds of 30 m/s, a ductile material separation is possible [12]. Adhesion of the machined material and abrasive wear on the cutting edge were identified as predominant wear-determining mechanisms. The use of cooling lubricant and higher cutting speeds (maximum 1000 m/min) reduce both forms of wear. Targeted cutting-edge rounding has a positive influence on the application behavior. Initial investigations have shown that tool coating using physical vapor deposition (PVD) of a titanium nitride (TiN) thin film increases the surface hardness and improves the cutting performance in turning the aluminum alloy EN AW 5754 [10]. For a subsequent deposition of a wear-resistant thin film on the natural rocks, this selection of rocks enables the consideration of various factors influencing the film properties and the adhesion behavior of the coatings to the substrate.

To improve the application behavior of the inserts made of rocks, the influence of the insert surfaces of the natural rocks, in particular their roughness, on the adhesion and the mechanical properties of the TiN thin films is investigated in this work. The aim is to obtain a comprehensive understanding of the effect of the interplay between rock type and surface roughness on the crystallographic structure, mechanical properties, and adhesion behavior of TiN. For cutting applications, TiN is a well-established and extensively studied thin-film material, typically deposited directly onto cutting tools. By selecting TiN, the results provide valuable initial insights into the behavior of PVD thin films on natural rocks and allow the development of adapted strategies for both the mechanical pretreatment of the natural rocks and the subsequent PVD coating process.

2. Materials and Methods

The natural rocks flint, lamellar obsidian, alta-quartzite, and silver-quartzite and the mineral quartz are examined in the presented study. The selected natural rocks differ both in their composition and in their mechanical properties. Previous studies have shown that the mechanical parameters the Vickers hardness and the fracture bending stress (Table 1) are particularly suitable for describing the load capacity and structural cohesion of the microstructure [5,6,9–12]. Their knowledge thus enables the comparability and the transfer of results to other rocks.

Table 1. Vickers hardness, fracture bending stress, and the thermal expansion coefficient (*TEC*), as well as the thermal conductivity of quartz, flint, lamellar obsidian, silver-quartzite, and alta-quartzite. The respective values for WC-6Co are given for comparison.

	Hardness [GPa]	**Fracture Bending Stress [MPa]**	***TEC* [C^{-1}]**	**Thermal Conductivity [W/(m × K)]**
quartz	13.9 ± 0.9	37 ± 7	2.43×10^{-7} [13]	2.52 [14]
flint	11 ± 4	58 ± 8	86×10^{-7} [15]	3.5 [16]
lamellar obsidian	9.1 ± 0.7	38 ± 5	61.6×10^{-7} [17]	8.4 [18]
alta-quartzite	15 ± 2	42 ± 5	0.9×10^{-7} [19]	5.69 [20]
silver-quartzite	14 ± 1	26 ± 4	16×10^{-7} [19]	5.69 [20]
WC-6Co	16 [21]	2313 [22]	55×10^{-7} [23]	140 [24]

The fracture bending stress was determined using a Zwick/Roell Kappa 100 DS (Ulm, Germany) universal testing machine following a three-point bending test (DIN EN ISO 7438 [25]). The hardness of the rock samples was analyzed using an automatic hardness tester of type QNESS Q10A+ according to the method of Vickers (DIN EN ISO 6507 [26]).

All rock samples were first cut into samples with dimensions of 20 × 20 × ~5 mm^3 using a Struers Discotom-10 (Ballerup, Denmark). The face grinding of these insert blanks was carried out using the Blohm Profimat MC 407 (Hamburg, Germany) and a 1A1 diamond grinding wheel ($d_{grinding\ wheel}$ = 300 mm) with a metallic bonding and a grain size d_{grain} of 46 µm and a grain concentration c_{grain} of 100 ct/cm^3. The cutting and feed speeds were 30 m/s and 50 mm/min, respectively, and the depth of cut was 0.05 mm. The inserts obtained their final shape via the Wendt WAC 715 Centro grinding machine. Metal-bonded diamond grinding wheels (d_{grain} = 46/91 µm; c_{grain} = 50/75 ct/cm^3) were used for the grinding process. The reader is referred to previous studies [5,6,9–12] for further details regarding the grinding of the rock inserts. In half of the samples, the rake faces were successively polished with a Tegramin-30 grinding and polishing machine using diamond polishing suspensions with grain sizes of 5 µm, 3 µm, and 1 µm.

The surface quality of the rake faces was determined using the arithmetic mean roughness *Ra* and the average roughness depth *Rz*. These surface parameters were determined using a tactile roughness tester of the Mahr Perthometer PGK type (Mahr GmbH, Göttingen, Germany). Additional characterization of the surfaces of alta- and silver-quartzite was carried out with an EVO 60 VP scanning electron microscope (SEM) (Zeiss, Jena, Germany).

The inserts were coated using an industrial PVD coating system, the METAPLAS.DOMINO kila flex (Oerlikon Balzers Coating Germany GmbH, Gladbach, Germany). The natural rock substrates were cleaned in an ultrasonic bath with ethanol for at least 15 min and were mounted on a substrate carousel with two-fold rotation and a rotation speed of 1 rpm for the rotating substrate table. Before the deposition process, its chamber was evacuated and heated to T = 400 °C. Subsequently, impurities were removed from the substrate surface by noble gas ion etching with arc-enhanced glow discharge (AEGD) for 15 min with a substrate temperature of T = 450 °C. The TiN thin film was synthesized using the direct-current magnetron sputtering (dcMS) method. For this purpose, a magnetron cathode was equipped with a monolithic titanium target (906 × 81 mm^2) with a target-to-substrate distance of 70 mm. The magnetron cathode power operated with P = 10 kW, corresponding to a power density of 13.63 W/cm^2, in an argon–nitrogen atmosphere with a substrate temperature of T = 350 °C. During the coating process, a constant bias voltage of U_b = −180 V was applied to the substrate table. The deposition time was set to 410 min to deposit TiN with a target layer thickness of 1.5 µm.

Due to the spalling of the TiN thin film on the polished rock surfaces, as later shown, and the inapplicability of conventional mechanical adhesion evaluation methods due to the heterogeneous structure of the natural rocks and a resulting outbreak failure, an alternative optical method was employed. This approach enabled an assessment of TiN adhesion on

various natural rocks with different surface roughness levels. In this regard, the samples were photographed using the DVM6 digital microscope (Leica Micro-systems GmbH, Wetzlar, Germany). The percentage area of the coating related to the total rake face area was calculated using the ImageJ image-processing software version 5.2. In the procedure, the spectral range of the TiN thin film was first selected and a binary image was created, in which the spectral range of the applied thin film is shown in black and the rest of the image in white (see Section 3). This approach ensured that only pixels corresponding to the specific TiN color, including areas with rough asperities and grooves, were converted to black, while the remaining pixels were transformed to white.

The in-house X-ray analyses were carried out using the Seifert Space Universal diffractometer (Eigenmann GmbH, Erlen, Switzerland). The instrument was equipped with a Co X-ray tube and, on the secondary side, with a 0.2° Soller aperture for the limitation of the angular divergence and a Ketek AXAS M detector system (Munich, Germany). The XRD data were measured from 5° to 80°, respectively 120° 2θ (CoKα) with 5 s per step (0.05°/step). The measurements of pole figures were carried out with a pole distance angle of α = 0° to 70° in 5° steps and an integral azimuth angle of 5° each in a range from 0° to 360° with a recording time of 5 s per step. The pole figures were analyzed with the software Labotex 2.1 (LaboSoft s.c., Krakow, Poland) [27]. The residual stresses were determined using the $\sin^2\psi$ method. The E-modules used to determine the residual stresses are listed in Table 1. The Poisson's ratio was assumed to be 0.25 for TiN. Furthermore, synchrotron radiation experiments were conducted at DELTA beamline 9 (Dortmund, Germany) [28]. The incident photon energy was set to E = 20 keV (λ = 0.619669 Å). The actual beam size on the sample's surface was 0.7 × 0.1 mm^2 ($h{\cdot}v$). The diffracted information was collected using an MAR345 image plate detector. The software package FIT2D version 18 [29] was used to calibrate the experimental setup and to integrate the collected 2D images [30]. As a calibrant, CeO_2 was used. The sample-to-detector distance was l = 333 mm.

The hardness and elastic modulus of the TiN thin films were evaluated using a nanoindenter G200 (Agilent Technologies, Santa Clara, CA, USA) operating in continuous-stiffness mode. The tests were conducted on polished natural rock substrates to ensure accuracy. For each substrate–film system, 49 indents were performed in a 7 × 7 matrix. To minimize substrate influence, the hardness values were derived from the maximum hardness of the indentation curves, with the indentation depth kept below 10% of the coating thickness.

3. Results and Discussion

The phase compositions of all natural rock samples are determined via powder X-ray diffraction analysis (Figure 1a). As expected, the XRD data of the mineral quartz show the characteristic reflections set for crystalline silicon dioxide (SiO_2) while the XRD data of lamellar obsidian solely show an amorphous hump around approximately 23° 2θ CoKα, typical for glassy SiO_2 compounds. In the XRD data of flint, solely SiO_2 reflections are identified. However, amorphous inclusions in the heterogeneous microstructure cannot be excluded. A secondary phase known in the literature is calcium carbonate ($CaCO_3$) [6]. SiO_2 reflections can also be detected in alta-quartzite and silver-quartzite. In both samples, additional reflections are observed; particularly the reflection at approximately 10° 2θ (CoKα) fits the monoclinic mineral phase muscovite ($C12/c_1$ (15)) well. However, the internal intensity ratios of the individual phases (SiO_2 and muscovite) mismatch the here-obtained XRD data of the natural rocks. For example, comparing the intensity ratio of the (100) and (101) reflections of SiO_2 observed for quartz and flint shows significant differences. A similar effect can be detected for the (200) and (114) reflections of the muscovite phase. These differences in the intensity ratios indicate either the existence of additional phase(s) or anisotropic crystallite sizes or the existence of a preferred orientation. All in all, the XRD analyses show the characteristic and complex heterogeneous microstructure of natural rocks. This heterogeneous microstructure complicates the determination of exact phase identifications as well as the fractional compositions. As a consequence, the additional

reflections in both quartzite samples cannot be doubtlessly identified as muscovite. Still, a layered aluminosilicate compound can be assumed as the secondary phase in both quartzite compounds.

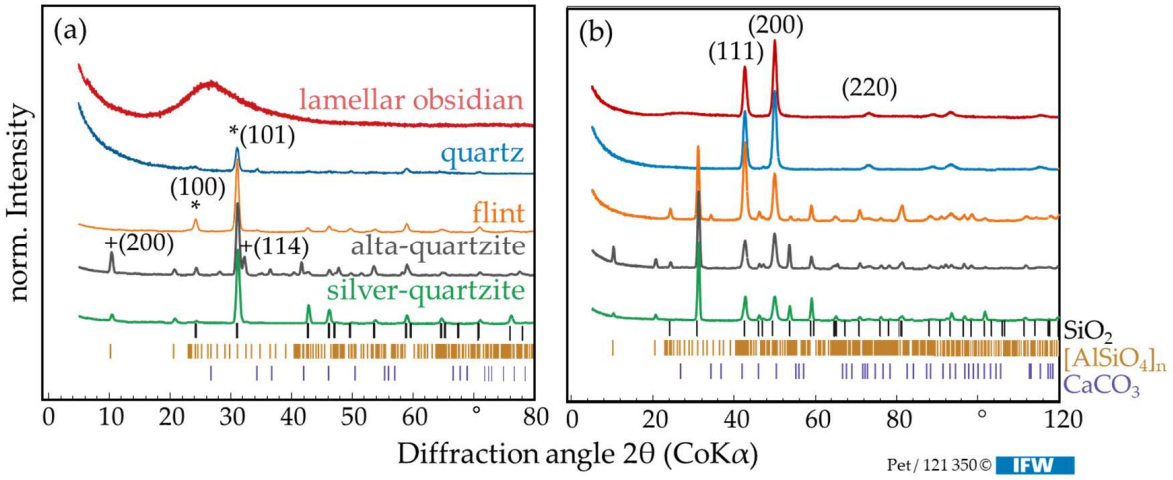

Figure 1. XRD data of all investigated natural rocks: (**a**) uncoated samples and (**b**) TiN-coated samples. The presented XRD data are normalized on the main intensity and shifted for the sake of clarity. The identified phases included in the heterogeneous microstructure of the rocks are indicated via tick marks: silicon dioxide (SiO_2, $P322_1$) [31], a layered aluminosilicate ($[AlSiO_4]_n$, $C12/c_1$) [32], and calcium carbonate ($CaCO_3$, $R\bar{3}c$) [33]. The (100) and the (101) reflections of SiO_2 as well as the (200) and the (114) reflections of muscovite are marked via an asterisk (*) and a cross (+), respectively. In (**b**), the three main intense reflections of the TiN coating are indexed.

Producing inserts made of rocks and their PVD thin-film coatability are in principle possible. It is generally known that the substrate's surface roughness affects the resulting adhesion behavior of applied PVD thin films. The arithmetic mean roughness *Ra* and the average roughness depth *Rz* are used as characteristic values for the surface quality of the inserts (Figure 2). The samples of the rock types quartz, flint, and lamellar obsidian show no significant differences in the surface parameters *Ra* = 0.55(4) µm and *Rz* = 3.9(3) µm with the selected grinding parameters. In comparison, the surface of both quartzite samples is rough with *Ra* = 1.1(1) µm and *Rz* = 9(1) µm. In addition, the observed standard deviation is high. However, by polishing the rock inserts, the surface quality can be increased and the characteristic values reduced on average to *Ra* = 0.04(1) µm and *Rz* = 0.5(1) µm for quartz, flint, and lamellar obsidian. Again, for the quartzite samples, rougher surfaces are observed with *Ra* = 0.4(1)–0.6(1) µm and *Rz* = 3.8(7)–4(1) µm.

The surface of the polished quartzite samples is analyzed via scanning electron microscopy (SEM) more closely (Figure 3). Major chunking can be identified in the micrographs of both samples. In addition, spherical particles in the heterogeneous microstructure of the quartzites are visible; these particles can be identified as an iron-containing phase. In the heterogeneous microstructure, additional calcium-rich areas are observed, which, through inclusion of the XRD analysis (Figure 1), are assumed to be calcites ($CaCO_3$). Because the reflections of the layered aluminosilicate compound overlap strongly with the reflections of $CaCO_3$, and because of the low $CaCO_3$ concentration, detection via XRD is not possible. During the polishing process, the whole $CaCO_3$ particles are pulled from the microstructural arrangement of the sample, leaving the observed cavities and scratching the surface.

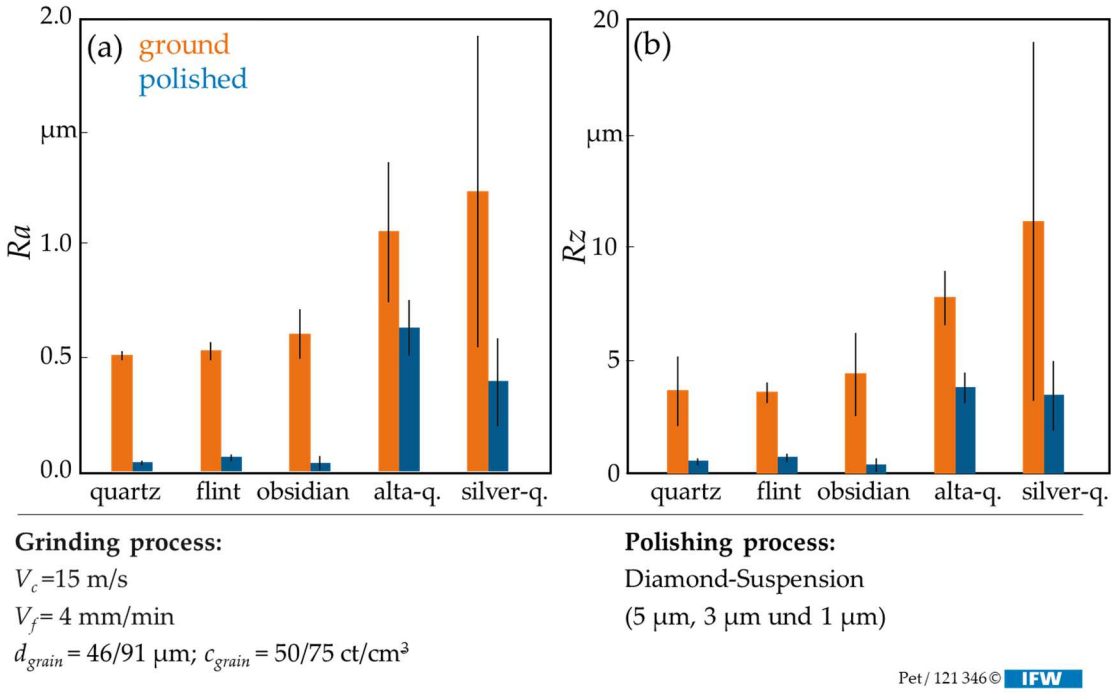

Figure 2. Averaged surface parameters (**a**) *Ra* and (**b**) *Rz* of the inserts made of rocks in the various process steps: after grinding (orange), after polishing (blue).

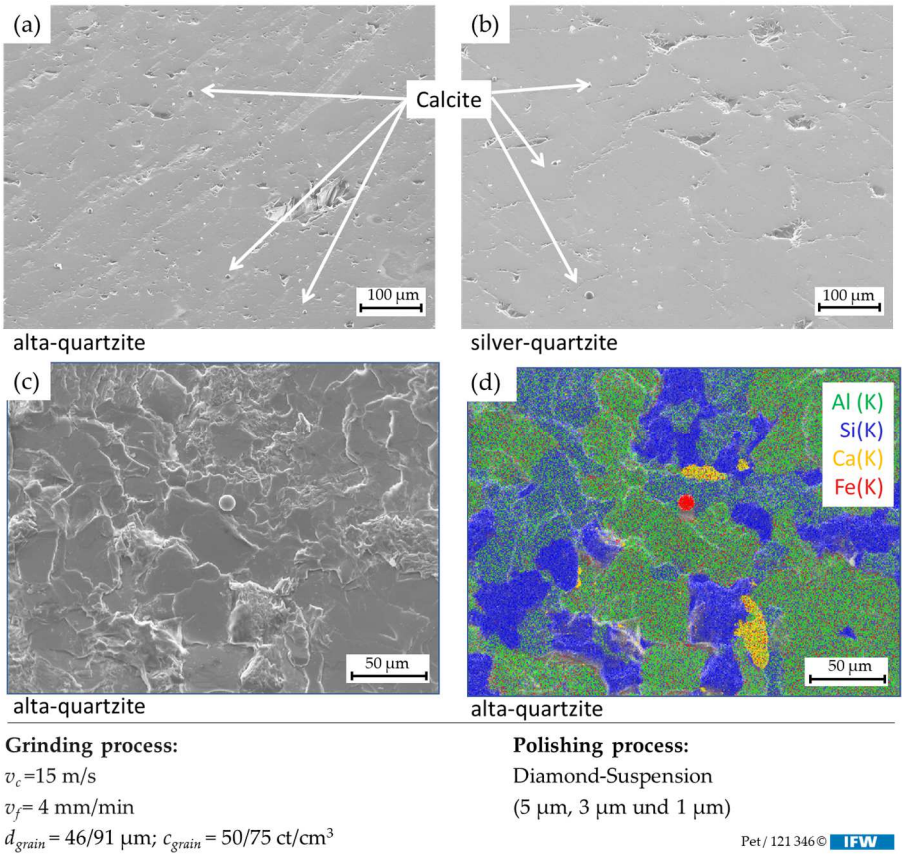

Figure 3. SEM micrographs of (**a**) alta-quartzite and (**b**) silver-quartzite after successive polishing. EDX analysis of alta-quartzite: (**c**) electron micrograph and (**d**) elemental mapping. The different elements are color coded.

The ground and the successively polished samples are coated with a TiN thin film using PVD. The ground substrates are completely covered with the TiN thin film, whereas large-film delamination occurs on the polished surface. In addition, it is not possible to evaluate the coating adhesion using conventional methods, such as the scratch test or the Rockwell indentation test, due to the heterogeneous and brittle nature of the rocks. Therefore, as an alternative approach, the percentage of the TiN thin-film area on the entire surface is determined and used as an indicator for the layer adhesion on the rocks. In principle, a distinction can be made between chemical, physical, and mechanical adhesion mechanisms [34]. While chemical and physical adhesions are based on the formation of chemical bonds or dipole interactions, mechanical adhesion is caused purely by mechanical interlocking in the interface between the substrate and thin film. Assuming that mechanical adhesion is the dominating factor for the good adhesion of the TiN thin film on the ground substrates, a decrease in layer adhesion would be expected with decreasing surface roughness. The rock inserts examined here show a strong dependence of the coating adhesion on *Ra* (Figure 4). For alta-quartzite and lamellar obsidian with ground surfaces and resulting *Ra* values between 0.47(1) and 1.2(2) µm, the surface coverage with TiN is between 80 and 100%. In contrast, lower TiN coverage is observed on quartz, silver-quartzite, and flint, despite similar or even higher *Ra* values. Additionally, it is observed that one sample each of polished quartz and obsidian shows 0% coverage. Although these samples were coated in the same batch as the others and were fully covered upon removal from the chamber, the TiN layer delaminates completely and is present only as loose powder on the surface. This may be due to insufficient cleaning in the ethanol bath prior to coating. For polished alta-quartzite with a *Ra* value of 0.63(1) µm, coverage ranges from 60 to 20%, depending on the sample, while other polished rocks, particularly with *Ra* < 0.1 µm, show lower coverage, below 50%. It is expected that, in addition to the mechanical adhesion mechanism, the chemical adhesion mechanism is also decisive for the layer adhesion of the TiN thin film on the rocks, as indicated by the greater coverage of TiN on lamellar obsidian and quartz. For smooth surfaces, chemical bonding is decisive, which can result in low adhesion due to different types of bonding in the substrate–layer interface.

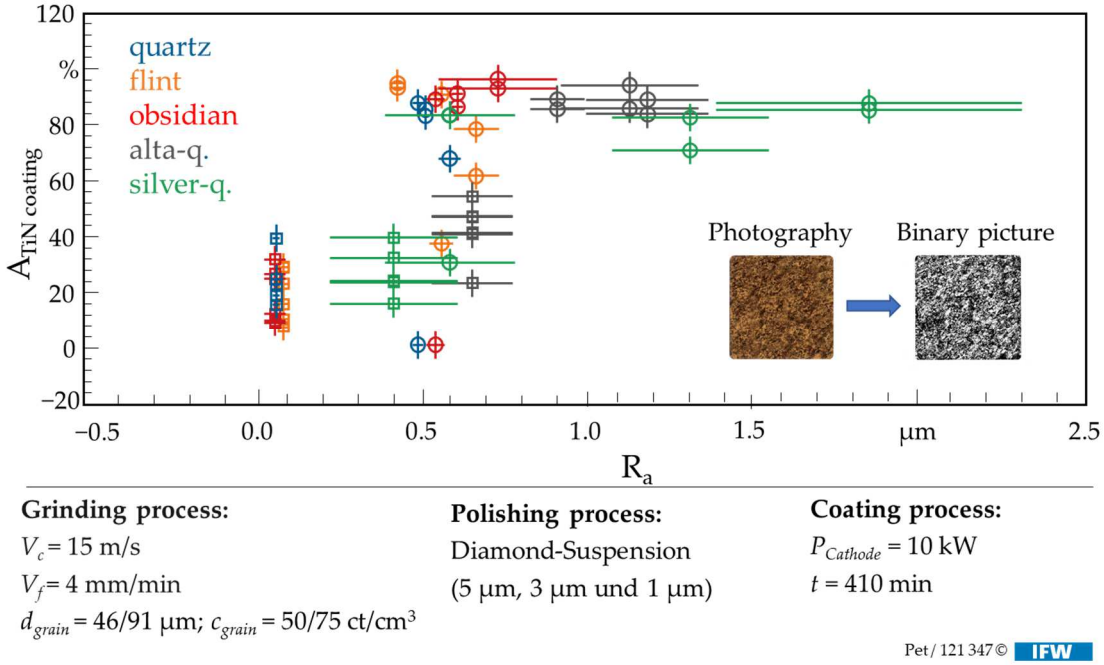

Figure 4. Percentage of the area of the TiN thin film in relation to the total rake face as a function of the arithmetic mean roughness *Ra*. The state of the substrate is indicated by the shape of the symbols.

The ground natural rock coated with a thin layer of TiN is analyzed via XRD (Figure 1b). Through the comparison of the XRD data collected from the sample with and without TiN thin film (Figure 1), the reflection set of face-centered cubic (fcc) TiN can be identified. In particular, the three main intense TiN reflections ((111), (200), (220)) can be identified in all samples. Comparing the intensity ratio of the (111) and the (200) reflections from the TiN, phase differences in the investigated samples are observed. As such, in most samples (lamellar obsidian, quartz, and alta-quartzite), the main diffracted intensity of the TiN phase is observed for the (200) reflection, while, in the XRD data of flint and silver-quartzite, the (111) reflection is most intense.

In Figure 5, the resulting two-dimensional diffraction data from the synchrotron experiments are shown. In the diffracted data of the uncoated lamellar obsidian, solely a diffuse scattered ring is observed (Figure 5a), typical for glassy SiO_2. As expected from the in-house XRD data (Figure 1), the reflections of hexagonal SiO_2 corresponding to orientations along the (100), (101), and (112) planes can be identified in the synchrotron data of all crystalline natural rocks. In the two-dimensional data of uncoated quartz, the SiO_2 reflections are detected as pronounced intensity spots (Figure 5c). Similarly, the two-dimensional data of the uncoated alta-quartzite and silver-quartzite show pronounced intensity spots on the characteristic Laue rings for polycrystalline materials. This phenomenon, the spot-like intensity (quartz), and the "dashed" Laue rings (alta- and silver-quartzite) are typical for materials with large crystallite sizes. The diffraction data of both quartzite samples show additional reflections caused by the layered aluminosilicate compounds. In the case of the uncoated flint sample, the detected Laue ring pattern is typical for a polycrystalline material with SiO_2 as the main phase. The two-dimensional diffraction patterns of all coated natural rocks show characteristic TiN reflections with an fcc structure next to the described reflections of the natural rock substrates. However, the locations of the substrate reflections of uncoated and TiN-coated quartz differ. This effect is typical for differently orientated large crystallites. The TiN reflections, in particular, the (111), (200), (220), and (311) reflections, show a distinctive intensity pattern. For all TiN-coated natural rocks, a similar intensity pattern of these TiN reflections is observed (Figure 5). Both the (111) and (200) reflections show a higher intensity at the azimuth angles of 45°, 90°, and 135°, while the (220) reflection is more intense in the range of 55° to 125°. The distinctive intensity pattern implies a strong texturing of the TiN thin film [35].

For further investigations, pole figures of all samples using the three main reflections ((111), (200), (220)) of the TiN thin film are measured (Figure 6). The lamellar obsidian itself shows no Bragg intensity, as such, the discussion of the intensity pattern is the most reliable. This detected pattern is characteristic for a fiber texture in the (111)- and (100)-direction. Unfortunately, the highly crystalline quartz, as well as the layered alta- and silver-quartzite samples, has reflections overlapping with the TiN reflection (compare Figure 1a,b), prohibiting the calculation of the multiples of a random distribution (MRD) factor. In the case of quartz, this is most severe, as is visible in the marked scattered intensities in Figure 6. However, a similar intensity contribution can be observed in all five analyzed samples. Consequently, all analyzed TiN thin films show a fiber texture. A quantitative comparison of all five samples is not possible due to this high scattering contribution of the quartz. Still, the ratio of crystallites in the different orientations ((111), (100), (110)) of the residual samples can be compared via the respective maximum intensities. In the thin films deposited on lamellar obsidian and alta- and silver-quartzite, these maximum intensities of the (111)- and (100)-directions are similar. Crystallites with these orientations are equally distributed in the films. However, in the TiN thin layer deposited on flint, approximately twice as many crystallites are oriented in the (111)-direction compared to the (100)-direction.

The microstructure of the TiN thin film and the surface integrity, as well as the interface of the thin layer on the different ground substrates, are investigated via scanning electron microscopy (SEM) images (Figure 7). The thickness of the TiN thin layers is approximately 1.5 µm. The analyzed TiN thin layers show columnar growth in the SEM

micrographs. Areas of good adhesion between coating and substrate are identified in the SEM micrographs. However, a local adhesive delamination of the thin layer is observed in all samples (Figure 7, marked areas). Interestingly, the TiN layer is locally detached from the substrate's surface but still intact. This indicates that the cohesion in the layer is strong enough that no cohesive layer failure is observed even though the adhesion towards the natural rock's surface fails. This supports the earlier observation that TiN exhibits low chemical bonding to the natural rocks. However, the high roughness of the ground surface ensures the mechanical interlocking, allowing TiN to adhere. In addition, a protrusion defect can be identified for the TiN-coated lamellar obsidian sample, which is commonly observed for PVD thin films [36]. Such defects are typically caused by surface irregularities or particles on the substrate, which serve as seeds and result in the thin film growing in the shape of an inverted cone that propagates through the film. In the case of lamellar obsidian, calcites may act as seeds for the growth of such nodular defects.

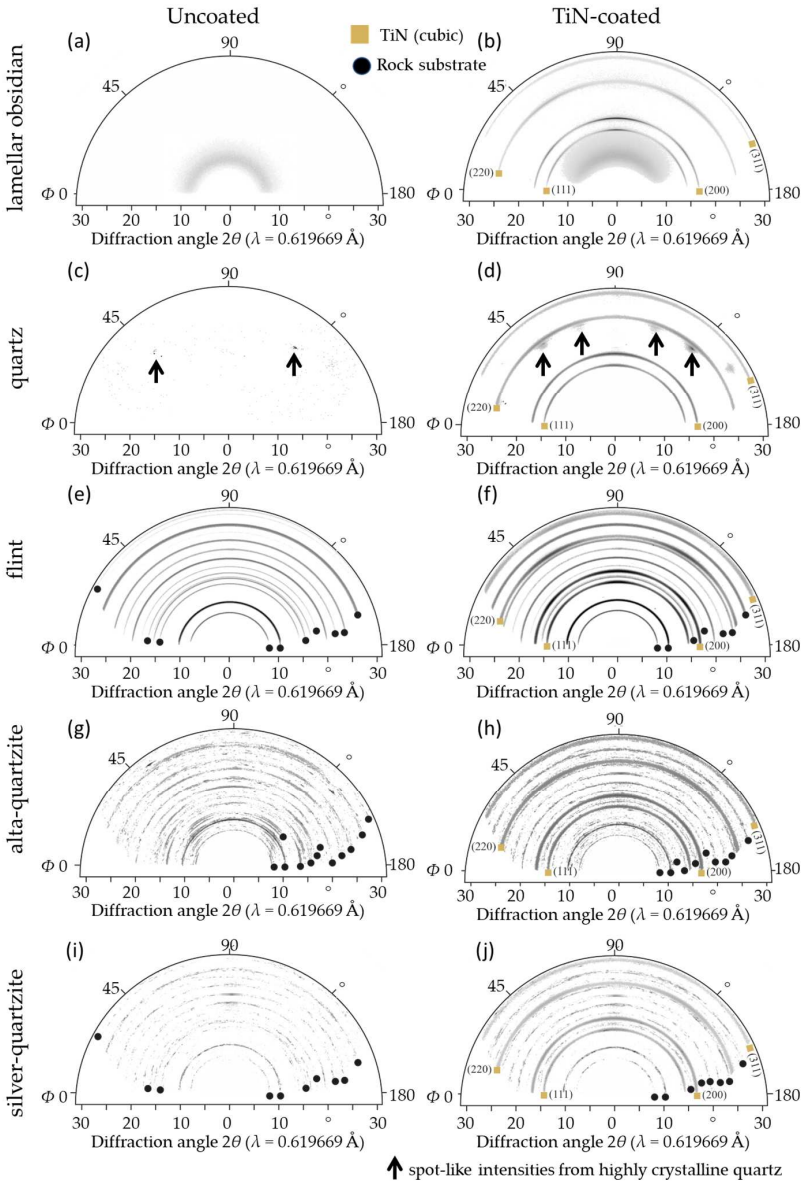

Figure 5. Two-dimensional diffraction pattern of different samples obtained by synchrotron experiments: (**a**) uncoated lamellar obsidian, (**b**) TiN-coated lamellar obsidian, (**c**) uncoated quartz, (**d**) TiN-coated quartz, (**e**) uncoated flint, (**f**) TiN-coated flint, (**g**) uncoated alta-quartzite, (**h**) TiN-coated alta-quartzite, and (**i**) uncoated silver-quartzite and (**j**) TiN-coated silver-quartzite.

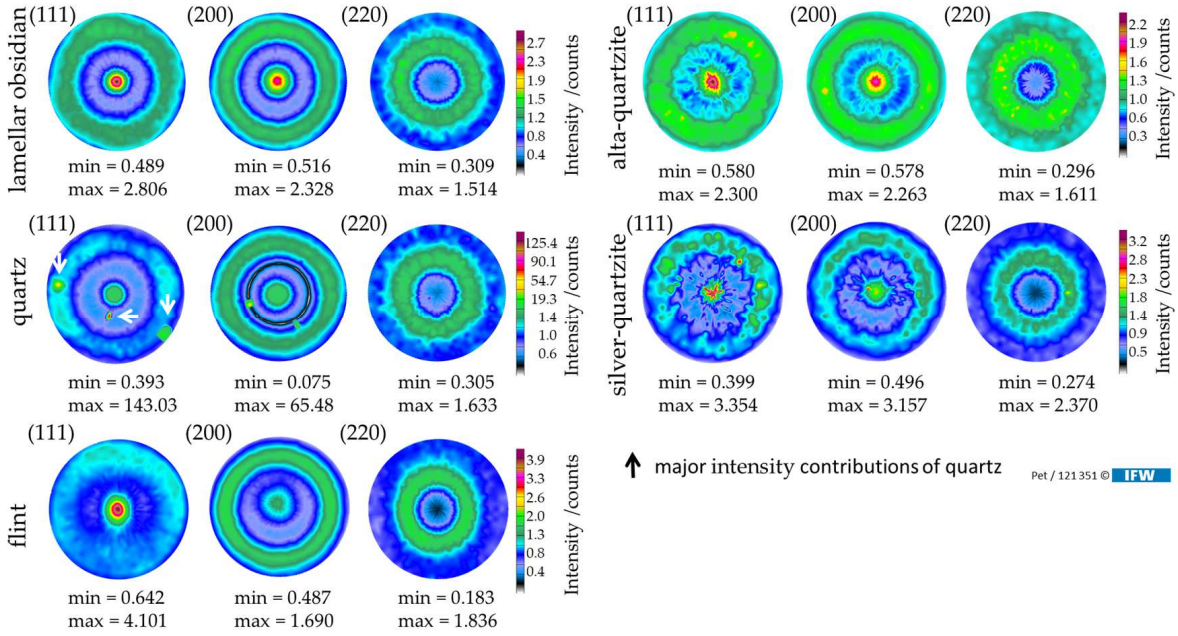

Figure 6. Pole figures of the TiN thin film applied on the investigated natural rocks. For all samples, the (111), (220), and (200) reflections were measured. Intensities originating from the natural rock substrate are indicated by white arrows.

In addition, the residual stresses in the TiN thin films are determined on the ground and coated indexable inserts (Figure 8). Because of the low thin-film adhesion on the polished rock samples, a meaningful investigation of residual stresses is prevented. All TiN thin films exhibit compressive residual stresses with values in the range of −550 to −800 MPa on lamellar obsidian, quartz, and silver- and alta-quartzite, while significantly higher compressive residual stresses of −1100 MPa are found for TiN on flint. The main component of all samples is SiO_2. Lamellar obsidian and quartz consist of non-crystallized or crystallized SiO_2 with inclusions. In addition, a layered aluminosilicate can be identified in both quartzite samples. The layered microstructure of the samples is oriented parallel to the flank face. Flint's microstructure is irregular, and, typically, flint can contain up to 14 wt.% calcite ($CaCO_3$) [37]. These different chemical compositions and microstructures cause differences in thermal conductivities and thermal expansion, which must be considered as both material properties may affect the stress state during the cooling procedure. In particular, a higher thermal expansion will result in higher compressive stresses upon cooling. The thermal properties of the different investigated natural rocks are listed in Table 1. According to a study by Kainz et al., TiN thin films exhibit a *TEC* of 89 × 10^{-7} °C^{-1} and a thermal conductivity of 45 W/mK [38]. In comparison, flint (*TEC* = 86 × 10^{-7} °C^{-1}) and lamellar obsidian (*TEC* = 61.6 × 10^{-7} °C^{-1}) have similar *TEC* values to TiN, while the other natural rocks are marked by lower values. In terms of thermal conductivity, however, the rocks have significantly lower values than TiN. However, a clear correlation between the thermal properties of the rocks and the residual stress state of the TiN thin film is not evident, as only flint shows remarkably different residual stress values. By considering the crystallographic structure of TiN, the texture analysis of the thin films (Figures 5 and 6) reveals that only the TiN thin film on flint shows significant differences in the orientation of TiN crystals. Indeed, the calculated pole figures of flint show that twice as many crystallites are oriented in the (111)- than in the (100)-direction compared to in the residual natural rock samples. The differences in TiN texture might explain the observed differences in the determined residual stress states, even though it seems that the latter effect of the TiN texture is predominant in this exact case. However, for more insights into the effects of the different chemical compositions and microstructures on the thermal properties, an in-depth analysis of the chemical compositions and microstructure with a subsequent investigation

of the thermal properties of each sample has to be performed due to the expected large heterogeneous nature of the samples.

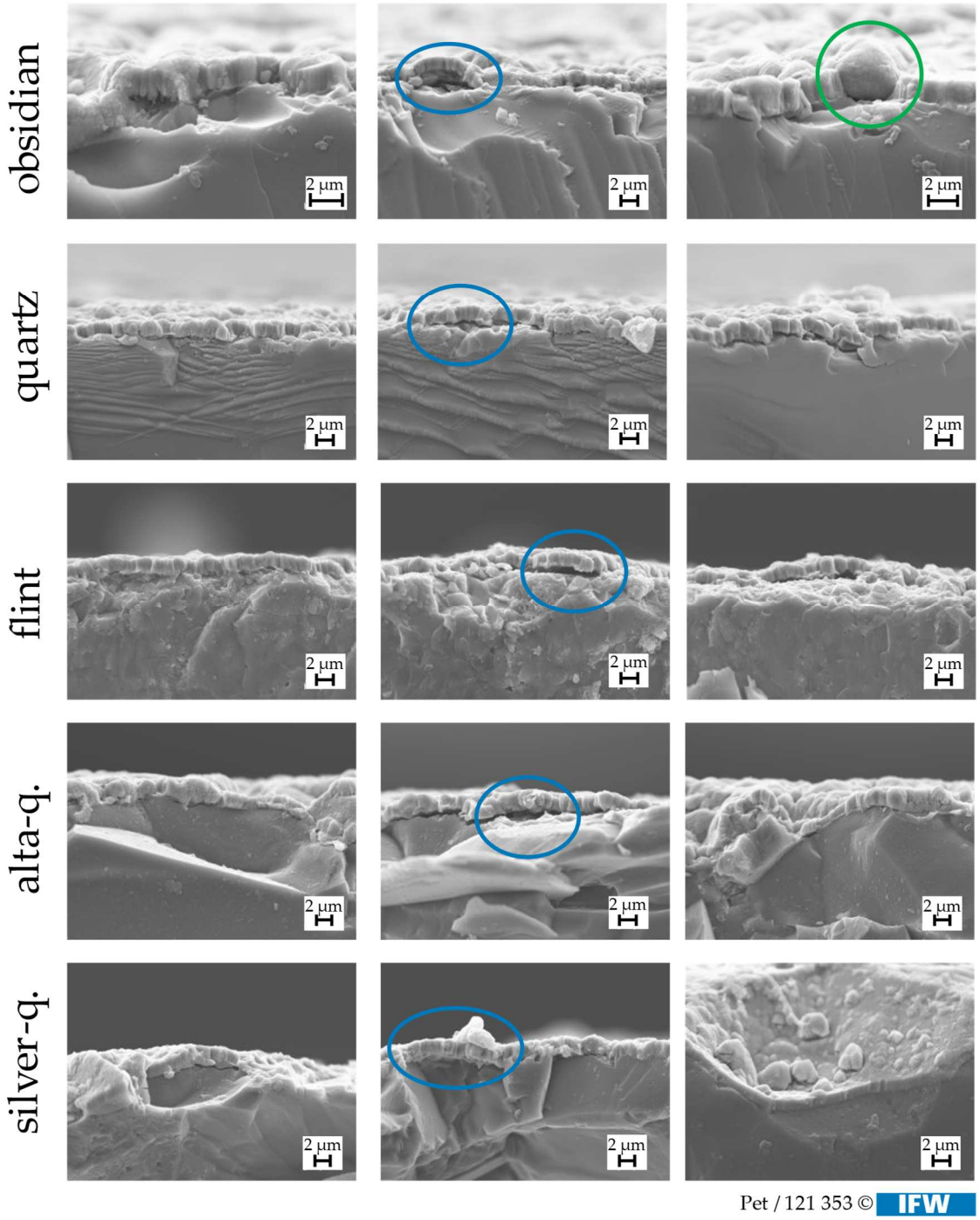

Figure 7. SEM micrographs of TiN thin film on lamellar obsidian, quartz, flint, and alta- and silver-quartzite. Adhesion failures of the thin film are marked in blue circles; a protrusion defect is marked in green.

The hardness and elastic modulus values of the TiN thin film on the polished natural rocks are presented in Figure 9. Compared to the uncoated natural rocks, the TiN thin films exhibit significantly higher hardness, confirming the effectiveness of PVD coatings in enhancing surface hardness. For most natural rock substrates, the hardness ranges from 21 to 22 GPa, except for lamellar obsidian, where a slightly higher hardness of 26 ± 2 GPa is

observed. A similar trend is seen in the elastic modulus, with TiN showing values between 185 and 202 GPa on most natural rocks, and a notably higher value of 266 ± 13 GPa on lamellar obsidian. The stress state does not appear to significantly affect the hardness of TiN. Instead, other structural factors, such as film density or crystallographic orientation, likely play a larger role in the mechanical properties of TiN on lamellar obsidian compared to other rocks.

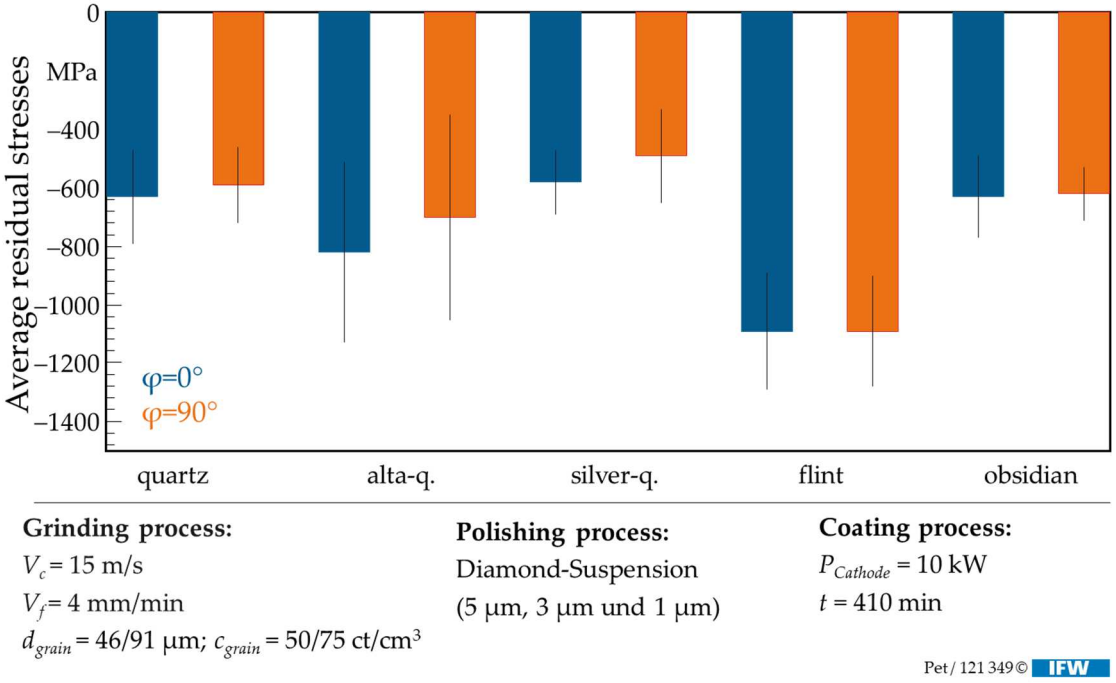

Figure 8. Average residual stresses of TiN coatings applied on the different rocks.

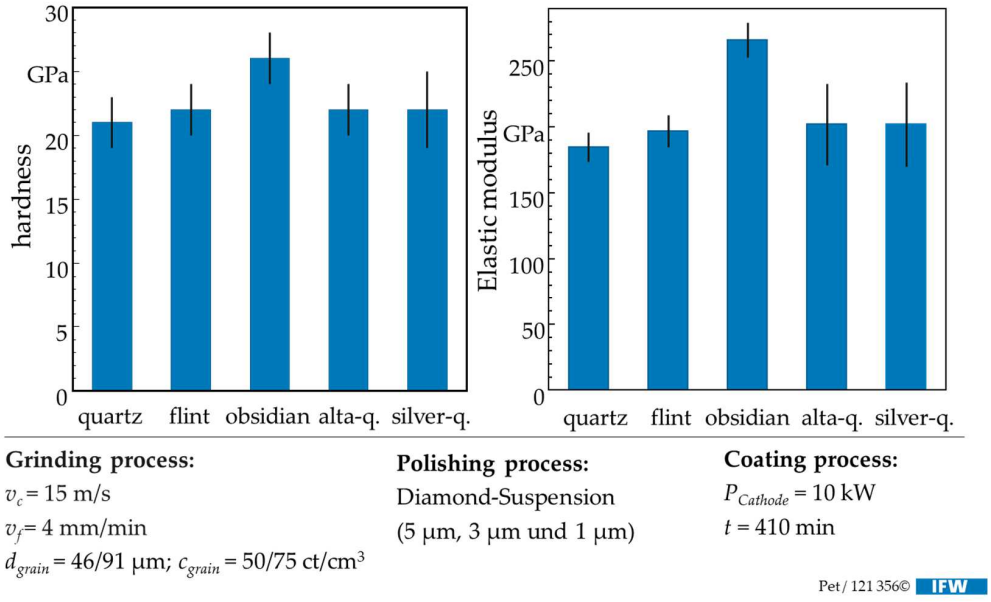

Figure 9. Hardness and elastic modulus of the TiN thin film deposited on of quartz, flint, lamellar obsidian, silver-quartzite, and alta-quartzite with polished surface, as obtained by nanoindentation.

4. Conclusions and Outlook

The ecological and economic challenges as well as ethical issues in carbide production can only be met by expanding the range of cutting materials. Here, inserts made of rocks can offer an alternative for machining soft materials. The presented research is

the first step in improving cutting properties, service life, and potential applications. A commercially used approach to improve the properties of cutting tools is PVD coating. The coatability of rock tools with TiN thin films is possible in principle. To optimize the thin-film adhesion on natural rocks, first insights on the effect of the interplay between surface roughness and rock type on the film properties are crucial. Good adhesion of the TiN thin film to the rocks is essential for coated inserts to achieve high performance and long tool life. We were able to show that adhesion to ground surfaces is mainly achieved by a mechanical adhesion mechanism so that the TiN film completely covers the surface of the substrate if high mechanical interlocking is possible. In this regard, a notably greater surface coverage of TiN was observed on grounded quartz and lamellar obsidian compared to on flint, alta-quartzite, and silver-quartzite. In contrast, the TiN film had a low adhesion on smooth, polished surfaces ($Ra < 0.5$ µm). However, in the SEM micrographs of the coated ground substrate samples, a failure of the thin film adhesion could be observed. To improve the adhesion between the substrate and the thin layer, the chemical adhesion has to be increased. For this reason, preparation approaches and the deposition process were investigated further to obtain an adjusted process route for improved adhesion of PVD thin films. In addition to an adapted coating process, intermediate layers with a high chemical affinity to the rocks and the TiN film can be used as adhesion promoters. The TiN thin films themselves are mainly formed by crystallites with the growth direction (111) and (100). While the ratio of both growth directions is close to one for quartz, lamellar obsidian, and both quartzites (silver- and alta-), a clear preference for the (111)-direction is notable for flint. All TiN films showed residual stresses in the compressive range between −550 and −800 MPa. The sole exception was flint. Here, significantly higher compressive residual stresses of −1100 MPa were found. Causes for these distinctive higher residual stresses could be the different chemical compositions of the natural rock, as well as its microstructures, which affect, in turn, the crystallographic structure of TiN and the resulting stress state. The residual stresses are not only interesting for the adhesion of the thin film but also affect the wear resistance during machining. High compressive residual stresses are advantageous for the susceptibility to scratch damage. However, a heterogeneous residual stress field, an alteration of compressive and tensile stresses, in the thin film or the interlayer between the thin film and the substrate may reduce the adhesion of the film. The relation between residual stresses and adhesion of the thin film will be closely investigated in a follow-up study. The TiN thin film effectively increased the surface hardness of the natural rocks, with values ranging from 21 to 22 GPa, except TiN on lamellar obsidian, which showed a higher hardness of 26 GPa. This suggests that the rock type influences further structural characteristics of TiN, which, in turn, affect its hardness and elastic modulus. For cutting applications, the high hardness of the TiN thin film is crucial for improving wear resistance, making it essential to further analyze the impact of substrate integrity on wear behavior and cutting performance in ongoing studies.

Author Contributions: P.D.H.W. and H.P. manufactured the indexable inserts. H.P. performed the analyses of the presented results and has written the manuscript. N.F.L.D. performed the PVD experiments and contributed to the discussion of the results. D.G. analyzed the synchrotron data. B.B. (Bernd Breidenstein) came up with the idea for the research. B.B. (Bernd Breidenstein) and W.T. acquired DFG funding for the project. W.T. and B.B. (Benjamin Bergmann) contributed to the conception and proofreading of the presented manuscript. All authors checked the information in the manuscript. All authors have read and agreed to the published version of the manuscript.

Funding: The investigations presented were funded by the German Research Foundation (funding numbers BR 2967/35-1 and TI 343/217-1) as part of the project "Development of PVD-coated tools made of rocks".

Institutional Review Board Statement: Not applicable.

Informed Consent Statement: Not applicable.

Data Availability Statement: The raw data supporting the conclusions of this article will be made available by the authors on request.

Acknowledgments: The authors thank the DELTA for providing synchrotron radiation and for the technical support of Christian Sternemann and Michael Paulus at beamline BL9 during the X-ray diffraction.

Conflicts of Interest: The authors declare no conflicts of interest.

References

1. Bobzin, R. High-performance coatings for cutting tools. *CIRP J. Manuf. Sci. Technol.* **2017**, *18*, 1–9. [CrossRef]
2. Denkena, B.; Dittrich, M.A.; Liu, Y.; Theuer, M. Automatic Regeneration of Cemented Carbide Tools for a Resource Efficient Tool Production. *Procedia Manuf.* **2018**, *21*, 259–265. [CrossRef]
3. Young, S.B. Responsible sourcing of metals: Certification approaches for conflict minerals and conflict-free metals. *Int. J. Life Cycle Assess.* **2018**, *23*, 1429–1447. [CrossRef]
4. Rizzo, A.; Goel, S.; Grilli, M.L.; Iglesias, R.; Jaworska, L.; Lapkovskis, V.; Novak, P.; Postolnyi, B.O.; Valerini, D. The critical raw materials in cutting tools for machining applications: A review. *Materials* **2020**, *13*, 1377. [CrossRef]
5. Wolters, P.; Picker, T.; Breidenstein, B.; Krödel, A.; Denkena, B. Application of natural rocks in cutting aluminum. In *Production at the Leading Edge of Technology*; Springer: Cham, Switzerland, 2021. [CrossRef]
6. Denkena, B.; Breidenstein, B.; Krödel, A.; Bergmann, B.; Picker, T.; Wolters, P. Suitability of natural rocks as materials for cutting tools. *SN Appl. Sci.* **2022**, *4*, 2. [CrossRef]
7. Wittke, W. *Rock Mechanics—Theory and Applications with Case Histories*; Springer: Berlin/Heidelberg, Germany, 1990.
8. Askaripour, M.; Saeidi, A.; Mercier-Langevin, P.; Rouleau, A. A Review of Relationship between Texture Characteristic and Mechanical Properties of Rock. *Geotechnics* **2022**, *2*, 12. [CrossRef]
9. Breidenstein, B.; Denkena, B.; Bergmann, B.; Wolters, P.; Picker, T. Turning Copper and Aluminum Alloys with Natural Rocks as Cutting Tools. *Materials* **2022**, *15*, 2187. [CrossRef]
10. Breidenstein, B.; Denkena, B.; Bergmann, B.; Picker, T.; Wolters, P. Tool wear when using natural rocks as cutting material for the turning of aluminum alloys and plastics. *Prod. Eng.* **2023**, *17*, 425–435. [CrossRef]
11. Breidenstein, B.; Denkena, B.; Wolters, P.; Keitel, M.; Tillmann, W.; Stangier, D.; Lopes Dias, N.F. A novel development of sustainable cutting inserts based on PVD-coated natural rocks. *Mater. Today Sustain.* **2023**, *24*, 100507. [CrossRef]
12. Denkena, B.; Breidenstein, B.; Bergmann, B.; Wolters, P. Investigation of the material separation behaviour of rocks using scratch tests for the design of tool grinding processes. *SN Appl. Sci.* **2022**, *4*, 157. [CrossRef]
13. Wei, Y. Thermal Expansion. In *Mineral Physics & Crystallography: A Handbook of Physical Constants*; Ahrens, T.J., Ed.; American Geophysical Union: Washington, DC, USA, 1995; Volume 2, pp. 29–44.
14. Shi, Y.; Chen, X.; Sun, C.; Xia, X.-L. Temperature-Dependent Thermal Conductivity and Absorption Coefficient Identification of Quartz Window up to 1100 K. *J. Therm. Sci.* **2022**, *32*, 44–58. [CrossRef]
15. SGP Inc. Available online: https://www.sgpinc.com/materials/soda-lime/standard-ar-flint/ (accessed on 5 October 2024).
16. Nahhas, T.; Py, X.; Sadiki, N.; Gregoire, S. Assessment of four main representative flint facies as alternative storage materials for concentrated solar power plants. *J. Energy Storage* **2019**, *23*, 79–88. [CrossRef]
17. Ericson, J.E.; Makishima, A.; Mackenzie, J.D.; Berger, R. Chemical and physical properties of obsidian: A naturally occuring glass. *J. Non Cryst. Solids* **1975**, *17*, 129–142. [CrossRef]
18. Gable, C.W.; Shankland, T.J. Radiative heat transfer in molten and glassy obsidian. *J. Geophys. Res. Solid Earth* **1984**, *89*, 7107–7110. [CrossRef]
19. Passion for Stones. Available online: https://material.passionforstones.de/file.php?prdPDF=1693 (accessed on 5 October 2024).
20. Wichert, J. *Slate as Dimension Stone: Origin, Standards, Properties, Mining and Deposits*, 1st ed.; Springer Mineralogy; Springer: Berlin/Heidelberg, Germany, 2022; pp. 61–134.
21. Yin, C.; Peng, Y.; Ruan, J.; Zhao, L.; Zhang, R.; Du, Y. Influence of Cr_3C_2 and VC Content on WC Grain Size, WC Shape and Mechanical Properties of WC–6.0 wt.% Co Cemented Carbides. *Materials* **2021**, *15*, 1551. [CrossRef]
22. Su, W.; Huang, Z.; Ren, X.; Chen, H.; Ruan, J. Investigation on morphology evolution of coarse grained WC-6Co cemented carbides fabricated by ball milling and hydrogen reduction route. *Int. J. Refract. Met. Hard Mater.* **2016**, *56*, 110–117. [CrossRef]
23. Habibi, F.; Mostafapour, A.; Heydarpour, K. Microstructural evaluation and mechanical properties of WC-6%Co/AISI 1045 steel joints brazed by copper, brass, and Ag-based filler metals: Selection of the filler material. *J. Adv. Join.* **2024**, *9*, 100212. [CrossRef]
24. *ISO 7438:2020*; Metallic Materials—Bend Test. Deutsches Institut für Normung e.V.: Berlin, Germany, 2020. [CrossRef]
25. *ISO 6507-1:2023*; Metallic Materials—Vickers Hardness Test—Part 1: Test Method. Deutsches Institut für Normung e.V.: Berlin, Germany, 2023. [CrossRef]
26. Kazymyrovych, V.; Kryzhanivskyy, V. Thermal properties of cemented carbides used for metal cutting. *Int. J. Refract. Met. Hard Mater.* **2023**, *111*, 106097. [CrossRef]
27. Pawlik, K.; Ozga, P. LaboTex: The Texture Analysis Software. Göttinger Arbeiten zur Geologie und Paläontologie, 1999, SB4. Available online: https://www.labosoft.com.pl/adc_method.html (accessed on 15 October 2024).

28. Krywka, C.; Sternemann, C.; Paulus, M.; Javid, N.; Winter, R.; Al-Sawalnih, A.; Yi, S.; Raabe, D.; Tolan, M. The small-angle and wide-angle X-ray scattering set-up at beamline BL9 of DELTA. *J. Synchrotron Radiat.* **2007**, *14*, 244–251. [CrossRef]
29. Hammersley, A.P. FIT2D: A multi-purpose data reduction, analysis and visualization program. *J. Appl. Crystallogr.* **2016**, *49*, 646–652. [CrossRef]
30. Rodi, D.J.; Mandava, S.; Gore, D.B.; Makowski, L.; Fischetti, R.F. Detection of functional ligand-binding events using synchrotron X-ray scattering. *J. Biomol. Screen* **2007**, *12*, 994–998. [CrossRef] [PubMed]
31. d'Amour, H.; Denner, W.; Schulz, H. Structure determination of alpha-quartz up to 68 $\times$ 10^8 Pa. *Acta Cryst. B* **1979**, *35*, 550–555. [CrossRef]
32. Guggenheim, S.; Chang, Y.-H.; Koster van Groos, A.F. Muscovite dehydroxylation: High-temperature studies. *Amer. Miner.* **1987**, *72*, 537–550.
33. Chessin, H.; Hamilton, W.C. Position and thermal parameters of oxygen atoms in calcite. *Acta Crystallogr.* **1965**, *18*, 689–693. [CrossRef]
34. Weiss, H. Adhesion of advanced overlay coatings: Mechanisms and quantitative assessment. *Surf. Coat. Technol.* **1995**, *71*, 201–207. [CrossRef]
35. Tillmann, W.; Hagen, L.; Stangier, D.; Lopes Dias, N.F.; Görtz, J.; Kensy, M.D. Lapping and polishing of additively manufactured 316L substrates and their effects on the microstructural evolution and adhesion of PVD CrAlN coatings. *Surf. Coat. Technol.* **2021**, *428*, 127905. [CrossRef]
36. Panjan, P.; Drnovšek, A.; Gselman, P.; Čekada, M.; Panjan, M. Review of Growth Defects in Thin Films Prepared by PVD Techniques. *Coatings* **2020**, *10*, 447. [CrossRef]
37. Graetsch, H.A.; Grünberg, J.M. Microstructure of flint and other chert raw materials. *Archaeometry* **2012**, *54*, 18–36. [CrossRef]
38. Kainz, C.; Schalk, N.; Tkadletz, M.; Saringer, C.; Winkler, M.; Stark, A.; Schell, N.; Julin, J.; Czettl, C. Thermo-physical properties of coatings in the Ti(B,N) system grown by chemical vapor deposition. *Surf. Coat. Technol.* **2020**, *384*, 125318. [CrossRef]